

CMB OBSERVATIONS WITH A COMPACT HETEROGENEOUS 150 GHz INTERFEROMETER IN CHILE

J. W. FOWLER, W. B. DORIESE,^{1,6} T. A. MARRIAGE, H. T. TRAN,^{2,7} A. M. ABOUBAKER, C. DUMONT,³ M. HALPERN,⁴
Z. D. KERMISH,² Y.-S. LOH,⁵ L. A. PAGE, S. T. STAGGS, D. H. WESLEY

Department of Physics, Jadwin Hall, Princeton University, P. O. Box 708, Princeton, NJ 08544.

Draft version October 29, 2018

ABSTRACT

We report on the design, first observing season, and analysis of data from a new prototype millimeter-wave interferometer, MINT. MINT consists of four 145 GHz SIS mixers operating in double-sideband mode in a compact heterogeneous configuration. The signal band is subdivided by a monolithic channelizer, after which the correlations between antennas are performed digitally. The typical receiver sensitivity in a 2 GHz band is $1.4 \text{ mK}\sqrt{\text{s}}$. The primary beams are 0.45° and 0.30° FWHM, with fringe spacing as small as 0.1° . MINT observed the cosmic microwave background (CMB) from Cerro Toco, in the Chilean Altiplano. The site quality at 145 GHz is good, with median nighttime atmospheric temperature of 9 K at zenith (exclusive of the CMB). Repeated observations of Mars, Jupiter, and a telescope-mounted calibration source establish the phase and magnitude stability of the system. MINT is the first interferometer dedicated to CMB studies to operate above 50 GHz. The same type of system can be used to probe the Sunyaev-Zel'dovich effect in galaxy clusters near the SZ null at 217 GHz. We give the essential features of MINT and present an analysis of sideband-separated, digitally sampled data recorded by the array. Based on 215 hours of data taken in late 2001, we set an upper limit on the CMB anisotropy in a band of width $\Delta\ell = 700$ around $\ell = 1540$ of $\delta T < 105 \mu\text{K}$ (95% conf.). Increased sensitivity can be achieved with more integration time, greater bandwidth, and more elements.

Subject headings: cosmic microwave background — instrumentation: interferometers

1. INTRODUCTION

Measurements of the CMB at small angular scales ($\ell > 1000$) complement those from *WMAP* (Bennett et al. 2003) and previous experiments including TOCO (Miller et al. 1999), BOOMERanG (Mauskopf et al. 2000; Ruhl et al. 2003), MAXIMA (Lee et al. 2001), DASI (Halverson et al. 2002), VSA (Grainge et al. 2003), and ARCHEOPS (Benoit et al. 2003), allowing yet more precise constraints on the standard cosmological model (Spergel et al. 2003). Additionally, such measurements will enable us to understand the transition from the linear to the non-linear growth regimes for the formation of cosmic structure. One promising measurement technique is interferometry because of the ability to control systematic errors. Existing CMB interferometers, CAT (Robson et al. 1993), CBI (Padin et al. 2001), DASI (Leitch et al. 2002), IAC (Dicker et al. 1999), VSA (Watson et al. 2003) are based on HEMT amplifiers (Pospieszalski 1992; Pospieszalski et al. 1995; Pospieszalski 1997) and operate at 30 GHz where the contamination from point sources can be large; MMIC technology at 90 GHz will enable a straightforward switch to higher frequencies. A compact interferome-

ter using SIS (superconductor-insulator-superconductor) mixers at $f > 100$ GHz has the potential to measure the CMB anisotropy and SZ effects where the point source contamination is at a minimum (Toffolatti et al. 1998) and where the SZ effect (Sunyaev & Zel'dovich 1970, 1972) has a characteristic spectral null. However, the technical complications are considerable, as might be surmised by the existence of only a few such interferometers (e.g., SMA, OVRO, BIMA, IRAM, NRO/NMA).

We have built and observed with a four element, heterogeneous, compact, fully-digital, SIS-based D-band (~ 145 GHz) interferometer designed as a prototype for a larger, more ambitious instrument. Novel elements of the interferometer include the channelizer, a custom microwave integrated circuit; digital correlators for CMB measurements; and mixed antenna sizes. We describe key features of the interferometer, the observations in Chile, and the data analysis.

2. THE MILLIMETER INTERFEROMETER

The Millimeter INTerferometer (MINT) is a compact instrument, approximately two meters on a side (without the ground shield) and cubical. All four receivers are mounted to a single rigid aluminum plate with fixed relative alignment. The plate sits atop a movable aluminum cage, as shown in Figure 1. The channelizer, digital correlators, data computer, and a calibration noise source are also mounted on the cage. By moving the entire signal path in unison, we avoid the potential phase changes that result from cable flexure and other moving parts.

The telescope cage moves on an altitude-azimuth mount. A linear actuator drives the telescope in elevation over the range 60° to 100° , controllable to the accuracy of the 17-bit encoder ($\sim 0.005^\circ$). The azimuth drive has

¹ Present address: NIST Quantum Electrical Metrology Division, 325 Broadway Mailcode 817.03, Boulder, CO 80305-3328.

² Present address: Department of Physics, University of California, Berkeley, CA 94720.

³ Present address: School of Medicine, University of Pennsylvania, Philadelphia, PA 19104.

⁴ Department of Physics and Astronomy, University of British Columbia, Vancouver, BC, Canada V6T 1Z4.

⁵ Present address: Center for Astrophysics and Space Astronomy, 389 UCB, University of Colorado, Boulder, CO 80309.

⁶ NRC Fellow.

⁷ Miller Fellow.

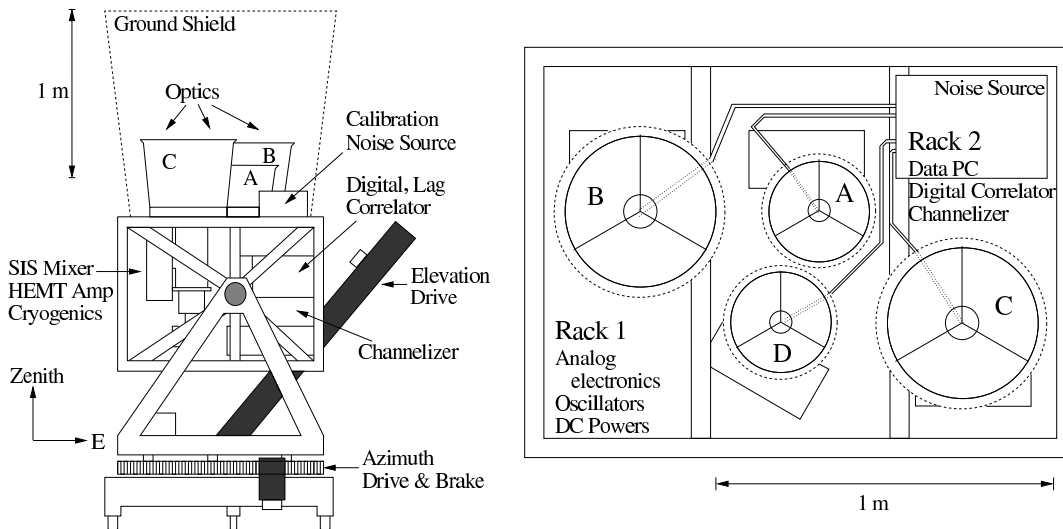


FIG. 1.— MINT interferometer. An elevation over azimuth mount positions the cage that holds four Cassegrain antennas. A ground shield mounted on top of the cage moves with the receivers. External to the cage, and not shown, are a thermal regulation system that servos the coolant for the RF electronics and correlators to ± 1 K, a position control computer, the helium compressors, and a 50 kW Katolight diesel generator to provide electrical power. The entire experiment fits inside one 20-foot shipping crate.

a range of 270° , with an inaccessible zone centered to the north. The azimuth is also instrumented with a 17-bit encoder and can be positioned to $\sim 0.015^\circ$ accuracy. A brake on the azimuth bearing allows us to turn off the electrically noisy azimuth drive during fixed-azimuth observing. A ground shield made of aluminum hex cell in the shape of an inverted frustum extends 1.2 meters above the receiver mounting plate. This shield prevents the receivers from illuminating the ground, either directly or through any number of reflections.

2.1. Optics and Receiver Arrangement

MINT uses antennas of two different sizes on its four receivers. A heterogeneous array is unusual in radio interferometry. It introduces complications such as complex effective beams and an “optical” phase that are undesirable in most astronomy applications. However, the faint CMB anisotropy is a weak signal at the limit of detectability. We maximize the sensitive area in the aperture plane of the four-element prototype array, within structural constraints, by combining antennas of two different sizes. Mounting the four antennas in a fixed configuration on a single plate also improves sensitivity by ensuring that the baseline separations in the (u, v) plane stay fixed as the sky rotates. Of course, deep observations of a single (u, v) visibility come at the expense of mapping.

An on-axis Cassegrain mirror system is mounted above each receiver. The inner two receivers have 30 cm diameter primary mirrors and 6.5 cm diameter hyperbolic secondaries. The equivalent focal length is 53.7 cm, giving a focal ratio of $f/1.8$. The outer two receivers have Cassegrain optics of the same shape but larger by a factor of 1.5 in each linear dimension. Rays from infinity focus near the entrance to a cold cylindrical feed horn⁸ inside the dewar. Identical horns with 17° FWHM beams

feed all four antennas. The feeds are characterized in Miller et al. (2002). The mirrors were machined from aluminum on a computer-controlled lathe. A rigid tripod of thin (1.6 mm) legs made of G-10 composite supports each secondary mirror (see Figure 1). A conical aluminum radiation shield with an opening half angle of 5° surrounds each primary mirror to a height of approximately one diameter. The shields are rolled outward at the top with a radius of $\sim 5\lambda$ to limit diffraction and reduce crosstalk between receivers.

The beam patterns of the two optical systems have been both measured and computed. Beam maps were measured using a chopped source (a 147 GHz Gunn diode with a D-band corrugated feed) and a diode power detector. The system allowed measurements over a dynamic range of 35 dB. Beams were also computed using the DADRA program (Barnes et al. 2002).⁹ From a spherical wave expansion of the field from a corrugated feed, DADRA computes the currents on the subreflector. Then, from the subreflector, it computes the currents on the primary. The net pattern is the sum of the fields from the feed, subreflector, and primary. We found it necessary to modify DADRA to include reflections from the primary back onto the secondary, because the MINT secondary mirror has a larger diameter than the hole in the primary. The small primary hole is desirable, as it puts power onto the sky rather than backward into the dewar, but it must be included in the computation. Extensive measurements on the MINT and similar Cassegrain antennas (e.g., Figure 2) confirm the computed beam shapes.

2.2. Receivers

The receiver is shown schematically in Figure 3. It uses the classic double-sideband superheterodyne configuration (Kraus 1986, e.g.). Other than the external optics,

⁸ Custom Microwave, Longmont, CO

⁹ YRS Associates: Y. Rahmat-Samii, W. Imbriale, & V. Galindo-Israel 1995, rahmat@ee.ucla.edu

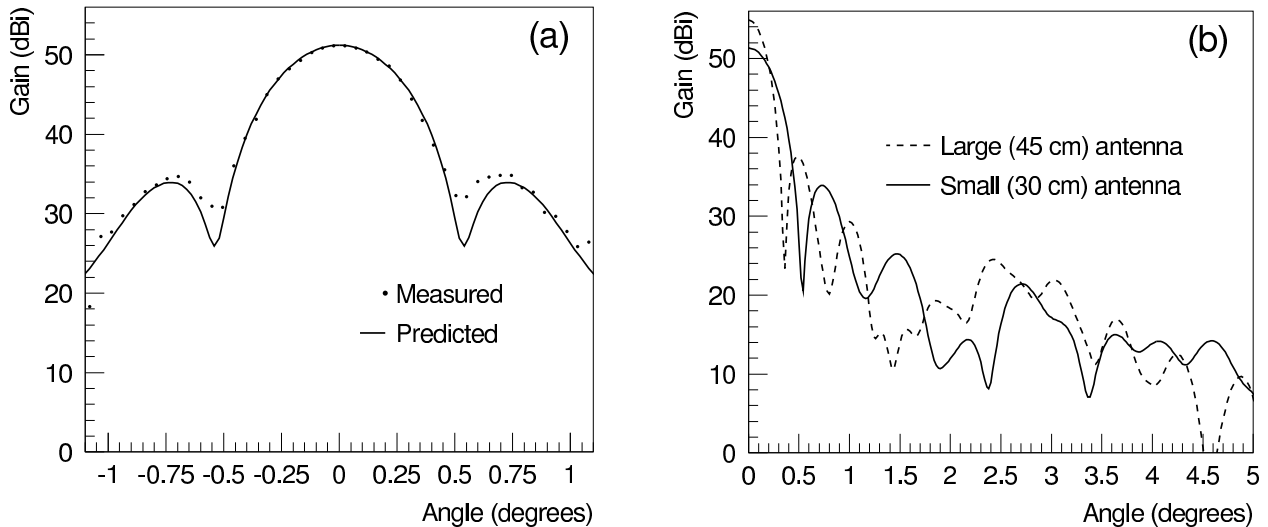


FIG. 2.— (a) Measured beam map of one of the small antennas. The dots are the measurement; the solid line is the DADRA computed beam, accounting for the defocus effect of measuring the beam at finite distance (36 meters). The data are normalized to the computed forward gain. Two-dimensional beam maps (not shown) confirm that the beams of both antennas are circularly symmetric. (b) Far-field beams, as computed by DADRA, for the small (solid) and large (dashed) antennas.

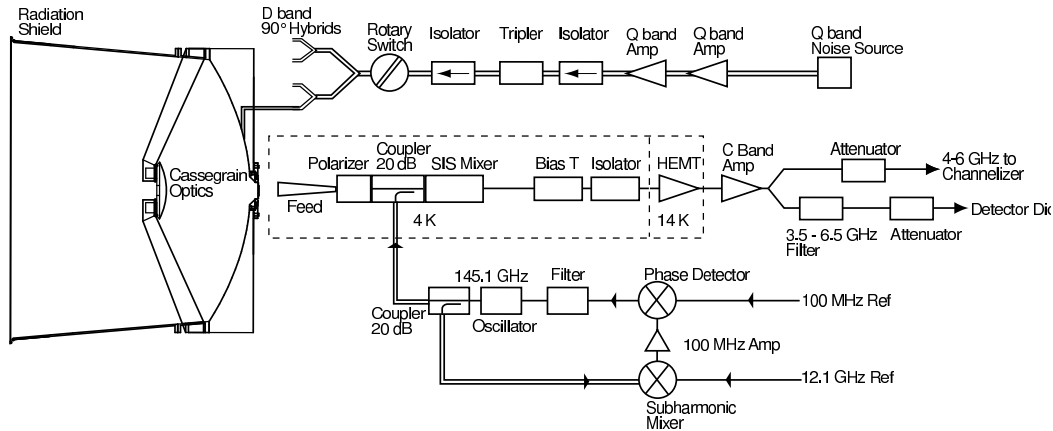


FIG. 3.— Schematic of the MINT RF chain, calibrator, and phase locking system. The noise calibrator is the top section; the sky signal flows from left to right in the center section; and the 145.1 GHz oscillator is produced and phase-locked in the bottom section. The dashed line surrounds cryogenically cooled components.

the four receivers are essentially the same. Celestial radiation is focused by the Cassegrain optics onto a single corrugated feed. The feed couples to a polarizer that accepts only right circular polarization. The output of the polarizer supports linear TE_{11} mode in a circular waveguide (diameter = 0.173 cm). A transformer (Padman 1977) converts it to TE_{10} in WR-5.8. The 1 mW local oscillator¹⁰ (LO) at 145.1 GHz is coupled to the signal waveguide at -20 dB through a NRAO branch-line coupler (Kerr et al. 1993). On the SIS junction, the LO (300 nW) and incident field (≈ 0.2 nW) are multiplied together.

For computing the optical transmission into the feed horn, the ambient-temperature, 0.056 cm polypropylene vacuum window; the 25 K, 0.052 cm thick z-cut quartz

IR blocker; and the 4 K backshort are treated as a single multi-layer system. The spacing between the elements and the thickness of the window and quartz were selected to maximize the transmission near 145 GHz.

Each SIS is cooled with a CTI-1020 CP refrigerator¹¹ modified with a third stage following the design of Plambeck, Thatte & Sykes (1993). The modifications were made by Cryostar.¹² The resulting refrigerators are efficient; each has a cooling power of 0.05 W at 4 K when driven by a 2.2 kW CTI 8200 compressor. The base temperature is approximately 3.7 K, but the temperature of the unloaded base varies by 400 mK peak-to-peak at 25 Hz, the operating frequency of the fridge. Reducing the variation with a high heat capacity, high conductivity

¹⁰ Zax Millimeter Wave Corporation, San Dimas, CA

¹¹ CTI, Helix Technology Corp., Mansfield, MA

¹² Cryostar Associates, Yuma, AZ

combination of stainless steel and copper and judicious choice of thermal breaks, we were able to servo the cold head temperature to ± 2 mK. This level of thermal stability was essential. Even with such temperature control, thermally driven dimensional changes in the cold head led to a small modulation of the reflection of the LO power from the vacuum window. The modulation could be monitored through $\sim 0.5\%$ variations in the SIS bias current.

The SIS was tuned with a backshort coupled through vacuum-tight gears to a computer-controlled motor outside of the dewar. The SIS is biased with a cryogenic NRAO bias-T, which outputs the RF signal. Following a 3.5–6.5 GHz cryogenic isolator,¹³ a 4.1 cm piece of stainless steel waveguide leads to an NRAO 3.5–6.5 GHz, 5–8 K noise temperature, 33 dB C-Band HEMT-based amplifier at 14 K. The output of the C-band amp feeds through stainless steel coaxial cable to the room-temperature electronics where it is amplified by another 52 dB. Half the signal is coupled to a total power monitor and the other half goes to the channelizer. With a 10 K thermal load as input (similar to the load observed in the field), the approximate level of the total power output is 1 mW.

Each receiver is tuned while coupled to a cryogenic, thermally controllable blackbody load that matches the feed but is electrically and thermally isolated from it. A LabVIEW computer program changes the load temperature, SIS bias voltage, and backshort position to find the optimal bias. In addition to the stable SIS temperature, the ambient electronics were stabilized to ± 0.1 K. Repeated tests of the system over multiple cool-downs showed that the optimal tuning position was stable. The same tuning procedure worked without changes for all four receivers (A, B, C, D). Table 1 gives the noise temperature of the SIS system in the four bands. After initial tuning, the SIS bias was not retuned during the observing season.

To provide a continuous relative calibration, we built a 138–142 GHz source that injects a broadband noise signal toward the subreflector of each telescope (Figure 3). A motor-controlled rotary mechanical switch ensured the “off” state of the source.

The LOs for all four receivers are phase locked to a 100 MHz master clock, which also drives the digitizers and correlators, the LOs in the channelizer and a 12.1 GHz reference signal for the LO locking. In the ambient-temperature electronics associated with each receiver, the 145.1 GHz LO is phased locked to the 12.1 MHz tone using a circuit based on one given to us by the SMA project (Hunter et al. 2002) at the Harvard Smithsonian Center for Astrophysics. Each circuit is based on a type II phase-locked loop, servoing on the twelfth subharmonic of the 12.1 GHz–145.1 GHz mixing product.¹⁴ The LO frequency is controlled by a varactor, an approach that requires far less current than the more usual Gunn bias does.

To summarize, the outputs of each receiver are a phase-locked 4–6 GHz IF signal and a total power monitor. The receivers were robust. They operated for a total of 30

receiver-months without failure. The receivers are described in more detail by Doriese (2002).

2.3. The Channelizers

The channelizers subdivide the 4–6 GHz IF (intermediate frequency) signal from each of the receivers into four 500 MHz bands, then downconvert each band to baseband. The channelizers are custom integrated microwave circuits designed using Agilent EEs of Advanced Design System software.¹⁵ Each circuit consists of a specialized layout of etched copper on 0.076 cm Duroid 6200 substrate and drop-in components. Its only connectors (apart from power supplies) are on the input and output. The channelizers are housed in a custom aluminum enclosure that provides isolation between adjacent channels and from the outside environment. The cavities between the traces and enclosure are coated with adhesive-backed, rubberized microwave absorber to suppress cavity modes. The channelizers for all receivers are mounted as a single, compact (6 cm by 30 cm by 30 cm), temperature-controlled unit.

The splitting is accomplished by a four-way power splitter composed of planar cascaded Wilkinson power dividers followed by planar bandpass filters. The Wilkinson splitters use a wide-band, three-segmented design (Li, Li & Bosisio 1984). Each bandpass filter is a six-pole Chebyshev type made from seven coupled microstrip sections (Matthaei, Young & Jones 1980). The realized bandwidth varies from band to band, between 400 and 600 MHz. There is no significant variation among the nominally identical bands in different channelizers.

Each filter is followed by a commercial surface-mount mixer,¹⁶ which downconverts the signal to baseband (0–500 MHz), and a surface-mount amplifier. Two local oscillator signals—one at 4.5 GHz and one at 5.5 GHz—are sufficient to mix the four separate bands to baseband. Thus half the bands are from the upper side-bands of the LOs and half are from the lower. The overall gain of the channelizer is ~ 12 dB across all four channels, with output power in the range +1 to +7 dBm. We label the bands out of the channelizer according to their IF frequency: red, yellow, green, and blue. The red band is 4.0 to 4.5 GHz in the IF, and thus nominally contains celestial information from both sidebands of the SIS: 149.1 to 149.6 GHz and 140.6 to 141.1 GHz. Tran (2002) gives further information about the channelizers.

2.4. The Digital Correlators

Each MINT digital correlator processes four 500 MHz-wide analog input signals, one from each receiver; all the red bands go to one correlator, for example. Incoming signals are digitized at 1 sample per nanosecond with 2-bit resolution. The correlator produces a 16-lag cross-correlation function, which is read into a data computer twice per second. An offline Fourier transform of the correlation function produces a cross-power spectrum with 62.5 MHz resolution. A total of four correlators are required to process all sub-bands. The basic design of the correlator was given to us by David Hawkins (Hawkins 2003).

¹³ Passive Microwave Technology, Inc., Camarillo, CA and P & H Laboratories, Simi Valley, CA

¹⁴ Pacific Millimeter Products, Golden, CO

¹⁵ Agilent Technologies, Palo Alto, CA

¹⁶ Mini-circuits, Brooklyn, NY

TABLE 1. NOISE TEMPERATURE OF FOUR RECEIVERS USING NRAO SIS MIXERS^a.

Band Name	IF Band (GHz)	T _A (K)	T _B (K)	T _C (K)	T _D (K)
Blue	5.5–6.0	40	33	68	29
Green	5.0–5.5	28	22	55	31
Yellow	4.5–5.0	24	19	33	27
Red	4.0–4.5	26	19	32	24

^aMeasured in the lab through the channelizer with a regulated blackbody load. The IF band is nominal band of the SIS output; the bandwidth for each is close to 500 MHz.

The electronics that compute the 16-lag cross-correlation functions between four analog signals are designed onto a single 38 cm by 38 cm, 8-layer, surface-mount circuit board. The four incoming signals are first processed by identical RF sections that each contain a variable attenuator, an amplifier, a low pass filter, and a voltage bias. The variable attenuators (M/A-COM model AT20-0107) have smallest steps of 0.5 dB. They are adjusted by data acquisition software to maintain the rms signal level into the digitizer near 0.28 V. This level optimizes signal-to-noise given our correlator algorithm and the digitizer quantization at ± 0.25 V (Cooper 1970). Resetting the attenuators hourly was found in field tests to be sufficient. The low-pass filters (Mini-circuits SCLF-550) have a -3 dB point at 605 MHz and block unwanted noise (particularly leakage of the channelizer LOs), which otherwise would be aliased into the signal. The voltage bias of -0.5 V is required by the digitizers.

The RF pre-processor is followed by a commercial 1 GSPS, 6-bit digitizer (SPT7610).¹⁷ The two most significant bits are passed to an ECL demultiplexer, which slows the signal rate to 62.5 MHz on a 32-bit bus. After conversion to LVCMOS, the 32-bit data streams from each receiver are fed into a single FPGA (Field Programmable Gate Array, XCV1000),¹⁸ which computes the correlation functions and communicates with a digital I/O card in the data PC. The FPGA also keeps a running count of the digitized values for each receiver—the “digitizer histograms.” These histograms, which are read out twice per second, proved very useful as monitors of the RF power reaching the digital correlator (see §3.2).

The algorithm for the correlator is built around a multiplier-adder kernel. The multiplier is implemented as a 4-bit lookup table, whose values are given by the 4-level, “deleted middle products” correlator algorithm. This table has a quantization efficiency of $\epsilon_q = 0.88$ relative to an ideal analog correlator (Cooper 1970).

The rack-mounted correlators for all receivers fit into a box 41 cm by 41 cm by 20 cm. Together the four consume 800 W and are cooled with a thermally regulated fluid. The correlators worked as designed throughout the 2001 campaign. More details are given by Tran (2002).

3. OBSERVATIONS

3.1. Cerro Toco Site

Observations were made from an altitude of 5200 m on Cerro Toco¹⁹ (longitude 67°47′09″ West, latitude 22°57′29″ South), a mountain overlooking the high Chilean Altiplano near the ALMA and CBI sites. This was the same site used for the MAT/TOCO experiment (Miller et al. 1999; Torbet et al. 1999). The mountain is accessible from San Pedro de Atacama, Chile, by four-wheel drive vehicle and can be reached from Princeton, New Jersey in 24 hours.

The atmosphere at the Cerro Toco site was often excellent. During the 38 calendar days of the campaign (2001 November 22 through December 29), twenty percent of potential observation nights were lost to overcast weather or snow. On the remaining usable nights, the effective atmospheric temperature at D-band was below 9 K half the available time. The first and third quartiles were 7 K and 13 K and the minimum observed temperature was 5 K. The typical opacity in D-band was therefore only a few percent. These temperatures exclude the contribution of the CMB and cover only the period from 23:30 to 10:00 UT each night (local time is UT−3). Data totaling 215 hours are used in the analysis presented here.

Two radio communication systems and automated observing software generally permitted remote operation of MINT from an apartment in the nearby town of San Pedro, 35 km away (Miller et al. 2002). One-way data transmission from the site (33 kbps data rate) allowed observers to monitor the data in real time. A separate, two-way, low-bandwidth system employed packet modems to relay commands to the telescope control computer.

3.2. Absolute Calibration

The digital correlator measures the quantity $\rho(\tau)$, the unitless correlation coefficient of two voltage signals as a function of lag τ :

$$\rho(\tau) \equiv \frac{\langle V_a(t)V_b(t+\tau) \rangle}{\sqrt{\langle V_a^2(t) \rangle \langle V_b^2(t) \rangle}},$$

where brackets represent averages over time t . The correlator output is converted from raw bits to ρ following §8.3 of Thompson, Moran & Swenson (1998). The next conversion, from ρ to correlated power or temperatures, requires knowledge of the overall system temperature of each receiver.

The most robust power calibration comes from the total power diodes, which measure power at the IF in a 3 GHz band (wider than but inclusive of the signal band).

¹⁹ The Cerro Toco site of the Universidad Católica de Chile was made available through the generosity of Prof. Hernan Quintana, Dept. of Astronomy and Astrophysics.

¹⁷ Signal Processing Technologies, Colorado Springs, CO

¹⁸ Xilinx Inc., San Jose, CA

Small nonlinearities in the diodes are characterized in the lab. The linearized voltage is calibrated in the field to the input temperature, using a combination of hot/cold load tests and sky dips. The hot load is a large piece of Eccosorb at ambient temperature ($T \approx 270$ K); the cold load is the sky at zenith. By measuring the sky power at a range of elevations, we separate the sky temperature, the receiver temperature, and the receiver responsivity (volts per Kelvin). The receiver temperatures and responsivities found in this way were consistent in three separate measurements taken at Cerro Toco over a three-week period. Assuming that responsivities remain constant, each diode serves as an independent monitor of the sky temperature. In practice, all four diodes found the same sky temperature to within 0.8 K rms, confirming that no other important contribution to the measured power varied significantly during the campaign.

The sky (atmosphere plus CMB) serves as a variable-temperature load, given the Eccosorb and sky-dip calibrations. The digitizer histograms give the power in each 0.5 GHz-wide sub-band. Together, the power and sky temperature permit an estimation of the receiver temperature and responsivity of each sub-band. Although the responsivity is found to change in one or a few discrete jumps during the campaign for some bands, the noise temperatures do not change significantly. Thus the total system temperature in each channel can be determined at any time simply by adding this constant receiver noise temperature to the varying sky temperature. The jumps, of approximately 10–20% in magnitude, occur only between nights and are attributed to problems in signal cables or their connectors.

This calibration method assumes that several key receiver properties stay constant: the responsivity of the total power diodes; the receiver temperature at the diodes; and the receiver temperature in each 0.5 GHz-wide sub-band. The redundant measurements of the sky temperature confirm these assumptions (Doriese 2002).

Observations of Mars and Jupiter are used to establish the forward gain (including optical efficiency) of the receivers. The gain is required to convert between brightness temperature and the fluctuations in the CMB physical temperature. Planetary observations are described in Section 4.

3.3. Relative Calibration and Phase Stability

The phase and amplitude stability of the interferometer are monitored using a switchable noise source. The noise is produced by a +20dB ENR Q-band source²⁰ followed by a series of amplifiers providing a gain of +70 dB. This signal enters an isolator, a frequency tripler, and another isolator (Figure 3). A D-band rotary waveguide switch (controlled by a stepper motor) allows the noise to be turned on or off. The signal is then split four ways by a 180° magic-T hybrid coupler and a pair of 90° short slot hybrid couplers. The resulting four signals are highly correlated, except that each is phase-delayed by 90° relative to the next. All components up to and including the power splitters are housed in a temperature-regulated box. Each signal travels through one meter of coin-silver D-band waveguide, where it is coupled into the telescope optics by an open-ended waveguide illuminating a tiny

“pickoff” mirror adjacent to the dewar window. Some power reflects up to the secondary and back into the dewar. The coupling efficiency is not measured but is found to be stable. The noise source is sharply cut off above 145 GHz by the bandpass of the Q-band amplifier, with the consequence that the noise contains D-band power only in the MINT lower sideband (139 – 141 GHz). This property is helpful in verifying the sideband separation procedure (§6.4).

During normal CMB observation, the noise source is switched on for 6–8 seconds out of every 450. A longer calibration of 30 seconds is performed every hour. The noise source produces power equivalent to 5–10 K in each receiver, so the correlated signal is observed with high signal-to-noise in a single 2-second integration period.

The magnitude of the noise signal recorded by the interferometer was stable throughout the campaign. On most nights, the fractional range of amplitudes was 3% (rms) or less in all bands and all baselines. Over the entire campaign, the rms range was 6%. Strong correlations in the amplitudes among all bands and all receivers suggest that the main source of amplitude variation was the noise source itself. For example, some variation is due to the waveguide switch failing to find the same resting spot on each repetition.

The phase stability of the instrument—a critical requirement for any interferometer—was also measured using the noise source and was found to be sufficient. Considered over the campaign, the measured phase variation over time and across frequency bins would cause average signal loss of 6% in most baselines (corresponding to an rms phase variation of 20°). The D-C and A-B baselines performed better than the others, with average loss of less than 3% and $\phi_{rms} = 12^\circ$. We attribute this difference to the power-splitting scheme in the noise source (A and B signals come from the same 90° hybrid), which permits a relative phase between the A/B signals and the C/D ones. This observation suggests that the calibration source itself is responsible for the main part of the observed phase variation over time. Therefore, the interferometer is more phase-stable than could be measured with this source (a comment that also applies to amplitude stability), and the 12° rms phase variation is an upper limit on the stability of the interferometer itself.

The instrument and sky noise is observed to integrate down with rms signal values scaling as $t^{-1/2}$ for averaging times t of up to 2000 seconds in a single night. Longer integrations were too few to make significant comparisons with the expected scaling law.

4. OBSERVATIONS OF THE SUN, MARS AND JUPITER

Repeated observations of the Sun were used to determine the telescope alignment throughout the Chile campaign. The receivers were temporarily covered with standard corrugated cardboard 2 mm thick to block the Sun’s optical and infrared radiation. The pointing was derived from separate maps of each receiver’s total power, not from interferometry. Common-mode pointing errors can be corrected off line and were determined to approximately 0.025° accuracy in elevation and in azimuth. Following an initial alignment of the receivers to each other (which also involved solar observations), they were found to be relatively aligned to within $\sim 0.02^\circ$. This angle corresponds to approximately 1/6 of the fringe spacing in

²⁰ Noise Com, Parsippany, NJ

the longest baseline. We noted no significant shifts during the campaign. At this level of accuracy, the flatness and placement of the cardboard shields appear to limit the measurements.

During the Chile campaign, Mars was visible nightly in the late afternoon and early evening. When weather and maintenance permitted, MINT observed Mars by repeatedly pointing the telescope ahead of Mars' position and allowing the planet to drift through the beam for 1–2 minutes. Approximately twenty hours of data were taken on or near Mars. Averaged over the season, the planet's angular diameter was $7''$. Using the 171 GHz temperature (Goldin et al. 1997) of 198 K, we expect Mars to produce antenna temperature in the small-small, mixed-size, and large-large baselines of only 1.9 mK, 2.9 mK, and 4.3 mK (the three baselines have forward gains of +51.3 dB, +53.1 dB, and +54.80 dB, according to the lossless optical model, and solid angles of $93 \mu\text{sr}$, $62 \mu\text{sr}$, and $42 \mu\text{sr}$). Jupiter was observed only at the end of the campaign.

The Mars data are used to measure the phase versus frequency profile of the instrument. Since Mars appears as an unresolved point source to MINT, its visibility phase should be a simple function of its position relative to the phase center of a given baseline. In particular, the phase should be nearly independent of the base-band frequency (effects of wavelength variation are small due to the small fractional bandwidth at D band). With the phase corrected for the position of Mars, a fiducial phase $\phi(\nu)$ is determined by averaging the complex visibility over many Mars observations. All data, including planetary calibrations and CMB data, are adjusted by subtracting the fiducial phase. After making this adjustment, it is possible to average complex visibility across all frequencies.

The visibilities measured on Mars match the important features of a point source. The visibility magnitude is approximately Gaussian (as a function of pointing angle away from the planet) with a width as expected from the primary beam widths. The visibility phase is also consistent with the expected $2\pi\mathbf{x} \cdot \mathbf{u}$ fringes. The phase of the setting Mars is stable over the campaign at the level of 5° – 10° rms, depending on the baseline. Even in the worst baseline, the computed signal loss due to the phase variation is only 3%. The phase is somewhat less stable during observations of Mars rising (10° – 20° rms, or 2%–10% loss), but these data are taken during daylight hours and are therefore less indicative of the instrument stability during its nighttime CMB observations.

Mars' visibility magnitude, though stable during the campaign, does not match the expected magnitude. For all baselines involving receiver A, the magnitude is only 33% of the expected value; for other baselines, the observation is 75% of the expected value. Extensive tests to explain the deficit were performed after MINT returned to Princeton in 2002. The tests involved direct observation of Jupiter, a high signal-to-noise source, and confirmed the signal loss. By switching equipment between the receivers, channelizers, and correlators, the deficit was localized to the poor performance of the circular-to-linear polarizers at the base of the feeds. The degradation is clearly evident only while observing a known celestial source interferometrically (which was not possible prior

to deployment). This loss of coherent signal is corrected at the end of the analysis pipeline by scaling up all average and rms values.

Jupiter was too low in the northern sky during late 2001 to be visible to MINT in its normal configuration. After the CMB campaign ended, the ground shield was removed and replaced by a flat mirror that covered all receivers. This mirror redirected the beams of each receiver by 76° in altitude, allowing observation of Jupiter. The planet's larger angular diameter ($47''$) makes the expected signal much larger than the Mars signal and easily discerned in a single 2-second data frame. We assume a brightness temperature of 172 K for Jupiter, given by *WMAP* measurements at 90 GHz (Page et al. 2003). The Jupiter observations (taken on consecutive mornings 2002 January 2–4) confirm all the main results of the lower signal-to-noise Mars data, including phase and amplitude stability, beam sizes, and the reduction in signal (particularly in receiver A) caused by the polarizers.

5. OBSERVING THE ANISOTROPY

5.1. Sky Scan Strategy

An experiment's sensitivity to CMB anisotropy depends on how the observing time is divided among fields on the sky. The statistically optimal division requires observing each field until a signal-to-noise ratio of one is achieved, then moving on to the next. For MINT, this meant maximizing the observing time on each field. We used a quasi-tracking strategy which combines the stability advantages of the sky drifting over a stationary telescope with increased integration time beyond a normal drift-scan. The telescope was repointed eight times per hour to observe the same strip of sky ($1/8$ hour wide in right ascension) repeatedly. Pointings were made at a fixed azimuth angle and a range of near-zenith elevations. Although fixed points in the sky curve across a range of azimuth, this effect was small for the limited range of elevations used.

Table 2 gives the location of the center of each strip used in the current analysis, both in ecliptic and in galactic coordinates. Although the fields near RA= 7^{h} and 8^{h} are within 10° of the galactic plane, they are located far from the galactic center and outside other major components. Additionally, the spectrum of diffuse backgrounds such as interstellar dust falls approximately as $\ell^{-1.5}$ (Gautier et al. 1992). The galactic contribution in the MINT fields at multipoles $\ell \gtrsim 1000$ is negligible.

The effect of scanning continuous strips is to acquire a series of complex visibilities with signal highly correlated between neighbors. Simulations show that sky strips $w = 1.875^\circ$ long observed with a Gaussian primary beam of width $\sigma_b = 0.19^\circ$ have the same statistical power for measuring sky variance as $n_{\text{spot}} = 4.5$ separate spots. The general relation for all three MINT beam sizes is found to be

$$n_{\text{spot}} \approx 1 + \frac{w}{2.8\sigma_b}.$$

5.2. Data Selection

The data used for CMB analysis are selected based on time of day, sky temperature, and nominal receiver operation. The noise source calibrations (§3.3) show that

TABLE 2. MEDIAN RIGHT ASCENSION^a AND GALACTIC COORDINATES FOR CMB FIELDS WITH AT LEAST 9 HOURS OBSERVING TIME^b.

RA (h,m,s)	b (deg)	l (deg)
1 3 42	-84.47	161.59
2 3 5	-72.68	202.49
3 2 40	-59.54	212.27
4 2 34	-46.34	218.46
5 2 26	-33.12	223.82
6 2 16	-20.24	229.17
7 2 8	-7.68	234.97
8 2 6	4.37	241.77
9 2 1	15.52	249.94
10 1 47	25.41	260.21
11 1 39	33.31	273.18
12 1 38	38.34	289.07

^aThe declination of each strip is $23^{\circ}2'14''$ south.

^bThe nominal fields are spaced evenly in right ascension. The coordinates given here are medians of the data surviving all cuts.

the system phase response is stable from 23:35 UT until 10:05 UT. These times correspond approximately to half an hour after sunset and twenty minutes after sunrise. Outside these times, the phase variations are likely due to thermal changes in the noise calibration waveguide (which is insulated but not thermally regulated). Although we believe that the instrument is more stable than the calibrator, there is no way to be certain, and data are rejected outside this window of 10.5 hours per night.

In addition, the data are cut when the sky brightness in D-band (including CMB) exceeds an effective temperature of 35 K. At higher temperatures, the linear relationship between sky temperature and measured rms visibilities breaks down. The sky brightness cut removes 3% of the otherwise valid data, which due to their high noise temperature would have only 1% of the statistical weight.

Instrument criteria include tests for locked PLLs, functional 4K refrigeration, and properly synchronized correlator readout. The total data set after all cuts is 215 hours long, representing 54% of the available nighttime hours. The weather and the instrument are responsible for approximately equal shares of the lost time.

6. ANALYSIS

6.1. Expected CMB Signal for a Heterogeneous Interferometer

MINT has both 30 cm- and 45 cm-diameter antennas, a configuration which produces high collecting area for the medium and longest baselines, where the CMB signal is small, while permitting the shortest baseline to be only 160λ . Put another way, the heterogeneous array fills a larger fraction of the antenna plane than would an array of small antennas alone.

Given a CMB power spectrum, the expected variance of the interferometer visibility is derived by Hobson, Lasenby, & Jones (1995) and White et al. (1999) for the case of identical receivers. We consider here the calculation for a heterogeneous array, which differs in that the effective beam and its Fourier transform are complex.

We work with a modified “temperature visibility” quantity, which corresponds to a brightness tempera-

ture averaged over the beam solid angle, rather than the usual flux density. This definition amounts to a re-scaling of the usual visibility by a constant factor $\lambda^2/(2k\Omega_B)$, where Ω_B is the beam solid angle. We make this non-standard choice even though MINT’s power levels are ultimately calibrated to the flux density received from point sources (Mars and Jupiter). We have found it convenient to work in sky brightness temperature, a quantity appropriate to a beam-filling source. In particular, this choice permits quick and transparent comparison with non-interferometric CMB experiments and their sensitivities. We use the label V_T to designate the modified visibility definition; all formulas for V_T can be multiplied by $2k\Omega_B/\lambda^2$ to yield the conventional visibility.

Ignoring the frequency dependence of the CMB brightness across MINT’s narrow band and making the flat-sky approximation for small fields of view, the complex temperature visibility V_T at location \mathbf{u} in the $u-v$ plane is

$$V_T(\mathbf{u}) \equiv \int \frac{d\mathbf{x}}{\Omega_B} A(\mathbf{x}) \Delta T_B(\mathbf{x}) e^{+2\pi i \mathbf{u} \cdot \mathbf{x}}, \quad (1)$$

where \mathbf{x} is the two-dimensional position in the plane of the sky (conjugate to \mathbf{u}), A is the primary power beam of the antennas (normalized to one at its peak), $\Omega_B \equiv \int d\mathbf{x} A(\mathbf{x})$ is the beam solid angle, and ΔT_B is the CMB brightness temperature fluctuation ($\Delta T_B = \eta_{RJ} \Delta T$). The Rayleigh-Jeans factor η_{RJ} converts small physical temperature fluctuations ΔT to brightness temperatures:

$$\eta_{RJ} \equiv \frac{\partial T_B}{\partial T} = \frac{\lambda^2}{2k} \frac{\partial B}{\partial T} = \frac{x^2 e^x}{(e^x - 1)^2},$$

where $x \equiv h\nu/(kT)$. At 145 GHz and for $T = 2.73$ K, $\eta_{RJ} = 0.59$. Note that the definition of temperature visibility (equation 1) leads to a magnitude of $|V_T| = T_B \Omega/\Omega_B$ for an unresolved source of brightness temperature T_B and solid angle $\Omega \ll \Omega_B$. This fact connects the CMB observations to the absolute calibration off of Mars.

Apart from constant factors, the visibility is the Fourier transform of the product of A and ΔT_B . By the convolution theorem, it is also the convolution of their transforms:

$$V_T(\mathbf{u}) = \frac{\eta_{RJ}}{\Omega_B} (\tilde{A} \otimes \widetilde{\Delta T})(\mathbf{u}).$$

Using this expression for temperature visibility, its expected covariance matrix has diagonal elements of

$$C^T \equiv \langle V_T^*(\mathbf{u}) V_T(\mathbf{u}) \rangle \quad (2)$$

$$= \left(\frac{\eta_{RJ}}{\Omega_B} \right)^2 \int d\mathbf{v} |\tilde{A}(\mathbf{u} - \mathbf{v})|^2 T_{cmb}^2 S(\mathbf{v}) \quad (3)$$

using the unitless power spectrum, $S(\mathbf{v})$, defined by

$$\langle \tilde{T}^*(\mathbf{v}) \tilde{T}(\mathbf{u}) \rangle = T_{cmb}^2 S(\mathbf{v}) \delta(\mathbf{v} - \mathbf{u}).$$

Note that the Fourier power spectrum S depends only on the magnitude of \mathbf{v} and approximately equals the spherical harmonic spectrum C_ℓ for large ℓ (if the spectrum is smooth enough): $S(v) \approx C_{\ell=2\pi v}$.

Non-diagonal elements of the theory covariance matrix are of two types. Two observations made by a single baseline but separated by angle Δ on the sky are accommodated with a factor $\exp(2\pi i \Delta \cdot \mathbf{v})$ in the integrand of Equation 3. Observations made by distinct baselines are also correlated. In the extreme case of parallel baselines (such as DA-BC and AC-DB in MINT), the correlation is complete. The MINT baselines of equal length but different orientations (such as DB and DC) are weakly correlated. The ratio of the magnitude of the covariance for DB-DC data to that of the DB-DB data is 18% for data from a single field ($\Delta = 0$), falling off quickly with increasing field separation Δ . The correlations between the short or the long baselines (DA or CB) and any other are negligibly small.

Analysis of the data is more easily done using the real and imaginary visibilities separately, leading to the final covariance elements

$$C_{RR}^T = \frac{(\eta_{RJ} T_{cmb})^2}{2\Omega_B^2} \int d\mathbf{v} |\tilde{A}(\mathbf{u} - \mathbf{v})|^2 S(\mathbf{v}) \cos(2\pi \Delta \cdot \mathbf{v}) \quad (4)$$

and

$$C_{RI}^T = \frac{(\eta_{RJ} T_{cmb})^2}{2\Omega_B^2} \int d\mathbf{v} |\tilde{A}(\mathbf{u} - \mathbf{v})|^2 S(\mathbf{v}) \sin(2\pi \Delta \cdot \mathbf{v}). \quad (5)$$

The other combinations obey $C_{II}^T = C_{RR}^T$ and $C_{IR}^T = -C_{RI}^T$. The new factor of 2 accounts for the fact that half of the sky variance appears in the real component of V and half in the imaginary. The two formulas are even and odd with respect to exchange of the two indexes (or equivalently, under reflection of Δ). This result can be generalized to give the covariance between distinct baselines.

In words, the covariance for $\Delta = 0$ is the sky power spectrum $S(v)$ averaged in two dimensions with a weighting function $|\tilde{A}(\mathbf{u} - \mathbf{v})|^2$. Recall that $A(\mathbf{x})$ is a single receiver's power beam, so $\tilde{A}(\mathbf{u} - \mathbf{v})$ is the autocorrelation of the voltage pattern in the antenna plane, offset from the origin by a distance \mathbf{u} corresponding to the baseline separation in wavelengths.

The complication of mixed antennas can be handled by extending the formulation of the antenna power reception pattern (Thompson, Moran & Swenson 1998). Starting instead with the voltage pattern $g_j(\mathbf{x})$ of antenna j for radiation from angle \mathbf{x} , the effective power beam A_e for baseline j - k is

$$A_e(\mathbf{x}) = g_j(\mathbf{x}) g_k^*(\mathbf{x}).$$

With this change, all formulas and statements above about A and \tilde{A} hold, except that $\tilde{A}(\mathbf{u} - \mathbf{v})$ becomes the *cross*-correlation of the two antenna's voltage patterns in the aperture plane. The resulting beam A_e is, in general, complex. The overall phase is unimportant; it merely adds to any other phase offsets in the system, which are measured by observing planetary point sources. Phase variation across the beam, however, adds an imaginary part to the beam A and its Fourier transform \tilde{A} . In MINT's mixed-antenna baselines, the phase of the effective beam is nearly constant well past the half-power point of the main lobe, so the imaginary part of \tilde{A} is of much smaller magnitude than the real part. Even so, the imaginary part is included in $|\tilde{A}|^2$ when numerically integrating equations 4 and 5, increasing the theory covariance by a few percent.

6.2. Approximate Analytic Expression for the Expected Signal

The theory covariance integrals can be approximated by taking the effective beams to be Gaussian and the power spectrum to be scale-invariant. The result is useful in illustrating how the CMB signal depends on instrument parameters. We assume a Gaussian beam with a beam solid angle $\Omega_G = 2\pi\sigma^2$. The ratio of the beam solid angles for the idealized Gaussian to the actual beam is akin to a main beam efficiency; call it $\epsilon_g \equiv 2\pi\sigma^2/\Omega_B$. The transform \tilde{A} of the normalized beam is then

$$\tilde{A}(\mathbf{u}) = 2\pi\sigma^2 e^{-2(\pi\sigma u)^2}.$$

Let

$$S(v) = \frac{1}{2\pi v^2} \left(\frac{\delta T^2}{T_{cmb}^2} \right),$$

so that δT^2 is a flat-bandpower temperature variance. Performing the angular part of the integral over $d\mathbf{v}$ (Equation 3) yields

$$C_{RR}^T = \frac{(\eta_{RJ} \epsilon_g \delta T)^2}{2} \int \frac{dv}{v} e^{-(2\pi\sigma)^2(u^2+v^2)} I_0(8\pi^2\sigma^2 uv),$$

where I_0 is the modified Bessel function of the first kind (Dieguez 1999; Hobson & Maisinger 2002). This can be simplified with the asymptotic expansion $I_0(x) \approx e^x/\sqrt{2\pi x}$ for large x . Defining $U \equiv 2\pi\sigma u$ and $V \equiv 2\pi\sigma v$,

$$C_{RR}^T = \frac{(\eta_{RJ} \epsilon_g \delta T)^2}{2U^2} \int dV \frac{1}{\sqrt{4\pi}} \left(\frac{U}{V} \right)^{3/2} e^{-(U-V)^2}.$$

Note that $r_P = \lambda/(2\pi\sigma)$ is the characteristic radius of the Gaussian power reception pattern in the antenna plane. Therefore, $U = \lambda u/r_P > 2$ for any real interferometer, as the separation λu must be larger than the antenna diameter. The integrand above is small except near $V \approx U$, so the divergence as $V \rightarrow 0$ can be ignored (it corresponds to an unphysical divergence in the CMB power spectrum at large angular scales, where the flat-sky approximation breaks down as well). For $U \approx 3.5$, the integral evaluates numerically to 0.54, approaching 0.500 in the limit of large U (large separation). Replacing the Gaussian beam width σ with the beam full width at half-maximum power $\theta_{FWHM} = \sqrt{8 \ln 2} \sigma$ (which is more readily generalized to non-Gaussian beams), the simplified estimate

for the covariance matrix is

$$C_{RR}^T \approx 0.27 \eta_{RJ}^2 \epsilon_g^2 \delta T^2 U^{-2} \quad (6)$$

$$\approx 0.038 \eta_{RJ}^2 \epsilon_g^2 \delta T^2 / (u\theta_{FWHM})^2. \quad (7)$$

Equation 7 can be used to estimate the magnitude of the CMB signal from any single interferometer baseline, given basic parameters such as baseline length and the beam width and efficiency. We expect that the ‘‘Gaussian efficiency’’ ϵ_g can generally be replaced with the main beam efficiency with little loss of accuracy.

6.3. Expected Signal-to-Noise on the Power Spectrum

A numerical evaluation of equations 4 and 5 gives a more accurate figure for the expected MINT variance per μK^2 of flat bandpower (Table 3). The two-dimensional Fourier transform of the beam, \bar{A} , is simplified by noting that the antennas and beams are symmetric about the optical axis. This symmetry reduces the problem to the one-dimensional Hankel transform of the radial function. The numerical result assumes the beam shapes computed by physical optics and confirmed by direct measurement (Figure 2).

The noise covariance C^N follows straightforwardly from the system temperature and the Dicke equation (Dicke 1946). The covariance of the real or imaginary output of a complex correlating interferometer is

$$C^N \equiv \langle \Delta T_B^2 \rangle = \frac{T_{sys}^2}{2\epsilon_q^2 \Delta\nu \tau},$$

where T_{sys} is the system noise temperature, ϵ_q is the efficiency factor of the digital quantization scheme, $\Delta\nu$ is the IF bandwidth, and τ is the effective observing time (see for example Thompson, Moran & Swenson (1998) eq. 6.42). Note that for MINT, τ is only half the elapsed time, because the phase-switching scheme effectively time-shares the correlator between measuring the real and imaginary parts of the correlation. Using a typical $T_{sys} = 45\text{ K}$ (including atmosphere and CMB), $\epsilon_q = 0.88$, $\Delta\nu = 1.9\text{ GHz}$, and 5 hours of observing time ($\tau = 9000\text{ s}$) on a CMB field, the noise covariance is $77\ \mu\text{K}^2$.

Using a set of $N \gg 1$ Gaussian deviates to estimate the variance of the set gives a fractional uncertainty of $\sqrt{2/N}$. The number of samples N is twice the number of fields observed, n_f , because the complex correlation at each field gives two independent samples. The variance $C^T + C^N$ of the data can be estimated to a fractional uncertainty of $1/\sqrt{n_f}$, so

$$\frac{\delta C^T}{C^T} \approx \frac{1}{\sqrt{n_f}} \left(\frac{C^T + C^N}{C^T} \right).$$

The two terms are the sample and noise variances. The quantity of interest, δT , is an rms rather than a variance; thus if the error is small, δT has half the fractional uncertainty of C^T . Consider the case of MINT observations, covering $n_f = 50$ fields. If sample and noise variance contributed equally to the final error (which is statistically optimal for a fixed total observing time), then the fractional error expected on the CMB signal δT would be $1/\sqrt{50} \approx 15\%$. Achieving this level of uncertainty would require 76 hours of observing per field, approximately 12 times the time actually available in the 2001 campaign.

6.4. Sideband Separation

The SIS mixers in MINT are inherently double-sideband devices, mixing sky signals in both ranges 139–141 GHz and 149–151 GHz down to a single IF band at 4–6 GHz. By switching a 90° phase shift in and out of the 145.1 GHz local oscillator tone every half-second, we separate the signals from the two sidebands. The separation is possible because an LO phase shift enters with opposite signs in the IF signals from the two sidebands. If C and C' are the correlation functions for unshifted and shifted data, then $(C + iC')$ and $(C - iC')$ isolate the contributions from lower and upper sidebands. This feature is preserved through the channelizer, where the signals are mixed down a second time. Thompson, Moran & Swenson (1998) describe the technique in §6.1. We have shown that their result generalizes to the cases of unequal power in the two sidebands and of lower sideband conversion at the second mixing stage.

The magnitude and phase of the cosmic signal should be nearly the same in both MINT sidebands.²¹ Therefore, it is not strictly necessary for CMB observation to distinguish the signals in the two bands. We could maintain a constant LO phase, effectively measuring only one component of the complex sky visibility. Instead, MINT determines the full complex visibility with half the observing time per component. The MINT strategy was chosen to characterize the instrument completely and to guard against possible drifts in the instrumental phase. Correcting such phase drifts—if measured by the calibration source (§ 3.3)—requires the complex visibility.

The sideband separation technique is proved in practice by observations of the calibration noise source. The noise source produces power only in the lower sideband of the MINT receivers. The measured cross-power spectra of the calibrator shows no power in the upper sideband except for small leakage near the band edges, a result of the limited number of time lags available in the correlation function.

7. ANISOTROPY RESULTS

7.1. Data Reduction

Analysis of the interferometer data is performed in Fourier (temporal frequency) space. First, the correlation function $\rho(\tau)$ is converted to brightness temperature (as described in §3.2 and §4). The conversion incorporates the results of sky dips and the absolute calibration determined from Mars observations. Using the sideband separation procedure, data with and without the 90° phase shift in the LO are combined to form a complex correlation function. The discrete Fourier transform of the 16-lag correlation gives the cross-power spectrum of one pair of antennas. Interpretation of the cross-power is complicated by the fact that both the lowest and highest frequency bins combine signal from upper and lower sidebands. This complication is not a problem, because MINT does not currently make use of the spectral information in analysis of the CMB data.

The ‘‘fiducial phase’’ $\phi(\nu_j)$ found from many Mars observations (§4) is subtracted from each data point.

²¹ The lower sideband power exceeds the upper by 7% for CMB fluctuations, owing to the frequency dependence in the conversion from physical to brightness temperatures.

TABLE 3. MINT BASELINES, BANDPOWER CONVERSION FACTORS, AND RESULTS OF 2001 CAMPAIGN.^a

Baseline	u	Beam solid angle Ω_B (μsr)	Beam FWHM θ_{FWHM} (deg)	Conversion factor, Gaussian ($10^{-3} \mu\text{K}^2/\mu\text{K}^2$)	Conversion factor, Numerical ($10^{-3} \mu\text{K}^2/\mu\text{K}^2$)	Effective ℓ for flat δT	Upper limit on δT (μK , 95% C.L.)
Short	169	93	0.445	4.3	4.3	980	232
Mixed ^b	260	62	0.348	2.5	2.4	1540	105
Long	492	42	0.297	1.1	1.0	3030	323

^aThe two conversion factors give the ratio of signal variance (in brightness temperature) to the CMB bandpower $C^T/\delta T^2$. For example, a bandpower of $1000 \mu\text{K}^2$ would produce a signal of $4.3 \mu\text{K}^2$ in the short baseline. Gaussian and Numerical columns refer respectively to the simplified estimate (Equation 7 in the text) and to the full numerical integration of Equation 4 used for the analysis. The conversions include several factors. The Rayleigh-Jeans factor squared is $\sim 1/3$. Signals separated into real and imaginary parts each contain only half of the anisotropy power. Use of a realistic beam instead of a “top hat” introduces a further factor of two in signal. Finally, the largest contribution, a factor of 15–60, comes from incomplete sampling of the u - v plane. The effective ℓ is the mean value probed if the power spectrum is flat. The last column gives the upper limits found by MINT on the CMB anisotropy.

^bThe conversion factors are per baseline. MINT has four baselines of the intermediate length $u = 260$.

The subtraction accounts for the constant phase variation across frequency of components such as imperfectly matched waveguides and amplifiers. The visibility magnitude is also divided by a template (based on planetary observations) to correct for gain variation across the signal band. With 16 lags and four separate 500-MHz sub-bands, the template for each baseline has 64 complex elements, which are determined once for the whole campaign by averaging the Mars results. Phase- and magnitude-corrected data are now directly comparable, and are therefore averaged across all 64 frequencies.

After all cuts, there are 390,000 two-second data records. Each record is a complex visibility (in brightness temperature) for each of the six baselines. The data show non-zero averages over the campaign of approximately 5–20 μK . These offsets do not vary significantly with time or with the observing elevation, so the six complex offsets are subtracted from the data records. Cross-talk between signal channels is the most likely cause of the small offsets.

CMB data are combined into bins of width 0.1° in right ascension (the bins are smaller in actual sky angle by a declination factor of $\cos \delta = 0.921$). All data are taken at fixed declination, so sky binning is required only in one dimension. The bin size is chosen to be the largest bin with nearly complete correlation of signal visibilities across its width. The visibility of a CMB signal varies across the bin with the usual $2\pi \mathbf{u} \cdot \mathbf{x}$ phase, but this position dependence is removed by “phase-centering” the visibility as if it had been observed at the center of the bin. Given a width of 0.1° , the signal lost due to averaging is only 1.5% in the longest baseline and 1.2% and 0.8% in the others, a loss which is accounted for by scaling the final results. The signal reduction would be closer to 10% for most baselines if the phase-centering correction were not made (the exception being the two baselines with u oriented north-south).

Combining the data within a bin entails finding the weighted average and the uncertainty on the mean, as given in Hobson, Lasenby, & Jones (1995). Each data point has a noise variance given by the 15-minute average of the visibility variance, scaled by the instantaneous system temperature to account for variation in the sky temperature on faster time scales. The rms estimated from this procedure matches the rms of the phase-centered

data to better than 2% for all baselines, when taken over the entire campaign. For the final likelihood analysis, the estimated “instantaneous rms” is scaled to eliminate the small mismatch.

Data from the identical baselines DC and BA could be averaged together at this point, but the large loss in Receiver A makes the BA data subject to unknown systematics and far less sensitive than the DC data; the AC data is likewise less sensitive than the BD data. We therefore discard the results from the BA and AC baselines.

7.2. Results

The time-averaged visibilities at each bin are our best estimate of the complex sky visibility on a 0.1° R.A. spacing. A maximum likelihood analysis (e.g., Bond, Jaffe & Knox (2000); Hobson & Maisinger (2002)) is used to find the flat bandpower in three distinct bands, corresponding to the MINT baseline lengths. The signal covariance matrix, given by equations 4 and 5, is computed numerically for the appropriate power spectrum ($S(v) \propto v^{-2}$) for all six baselines, and for all possible separations Δ from zero to 3° in 0.1° steps. For this computation, the beam transform $\tilde{A}(u)$ comes from the physical optics code. The DB-DC correlation of 18% is included in the covariance matrix, but the small covariances between baselines of unequal length ($< 1\%$ in all cases) are ignored. Because the scan strategy concentrated on 2° strips spaced every 15° , the signal covariance is block diagonal with approximately 18 separate blocks (of the 24 possible blocks, six correspond to areas of the sky high during the afternoon, which were not observed). The noise covariance matrix is diagonal. These simplifications make the total covariance matrix easy to invert.

Table 3 gives the 95% confidence level upper limits determined by MINT in the 2001 campaign. We compute the likelihood \mathcal{L} as a function of flat bandpowers δT , given a uniform prior distribution. The three baseline lengths are analyzed separately, as the correlations between them are in this case small enough to ignore. The separate likelihood functions of the mixed baselines are added, as their data are uncorrelated in u - v space. We define the upper limit so that the integral of \mathcal{L} up to the limit is 95% of the integral over the whole domain. The mixed baselines ($\ell \sim 1540$) provide the strongest limit,

105 μK , on the CMB anisotropy.

8. CONCLUSION

The Millimeter Interferometer has operated successfully as a prototype for a high-frequency CMB instrument. MINT combines heterogeneous antennas, double-sideband SIS mixers, monolithic channelizers, and digital correlators. All of these elements may be features in future CMB interferometers. To make a competitive detection of the CMB anisotropy, such an instrument would require wider bandwidth, longer observing time, and more receivers (having more distinct baselines would also improve the sampling in ℓ -space). Usable bandwidth in the D-band is ultimately limited by atmospheric emission lines (Matsushita & Matsuo 2003), but sideband-separating mixers—under development at NRAO (Kerr, Pan & Leduc 1998)—offer an instant factor of two improvement, given equal system noise temperatures. Consider an improved MINT, with 8 GHz bandwidth (4 GHz upper and 4 GHz lower sideband), four times the actual 2001 observing time, and fully working polarizers. Assuming 50 separate fields of view and the power spectrum of the 2002 WMAP best fit ΛCDM model (Spergel et al. 2003), the MINT window functions produce CMB bandpowers of 1450 and 590 μK^2 at effective $\ell = 900$ and $\ell = 1390$. In this case, the improved MINT would have the raw sensitivity to see anisotropy at the level of 7σ and 6σ in the short and medium baselines. We conclude that the techniques described here constitute a promising, if challenging, method for observing CMB anisotropies at or above 100 GHz.

We gratefully acknowledge design and construction help from Dave Wilkinson, Norm Jarosik, Ted Griffith, Laszlo Vargas, Bill Dix, Glenn Atkinson, Stan Chidzik, Elvis Dieguez, Jamie Hinderks, Mark Tygert, Michael Levi, William Magrabe, Ariel Lazier, Long Tran, Mark Morales, Paul Oreto, and Michael Nolta. MINT was made possible by SIS mixers designed by Tony Kerr, phase-locked loops modified from a design of Bob Wilson and Robert Kimberk, cold heads designed by Dick Plambeck, and a digital correlator modified from a design of David Hawkins. These colleagues freely offered design advice and guidance. Agilent provided a complimentary educational license for EEsof design software. Mark Devlin loaned us his telemetry system. Angela Glenn and Kathleen Warren assisted in countless ways, which included purchasing equipment, producing this document, and getting MINT and the authors to Chile. Operating in Chile was possible through the efforts of Angel Otárola and Roberto Rivera. Use of the Cerro Toco site was made possible by Hernan Quintana. For additional assistance in Chile, we thank Gaelen Marsden, Juan Burwell, the entire CBI team (particularly for help when our truck broke down), Ocegtel SA, and the staff of La Casa de Don Tomás. We thank an anonymous referee for comments which helped us to improve the paper. This work was supported by an NSF NYI award, a Robert H. Dicke Fellowship to JF, a David and Lucile Packard Fellowship to LP, an NSF Graduate Fellowship to TM, and NSF grants PHY96-00015 and PHY00-99493.

REFERENCES

- Barnes, C., et al. 2002, *ApJS*143, 567
 Bennett, C. L., et al. 2003, *ApJS*, 148, 1
 Benoit, A., et al. 2003, *A&A*, 399, L25
 Bond, J. R., Jaffe, A. H., & Knox, L. E. 2000, *ApJ*, 533, 19
 Cooper, B. F. C. 1970, *Aust J Phys*, 23, 521
 Dicke, R. H. 1946, *Rev Sci Instrum*, 17, 268
 Dicker, S., et al. 1999, *MNRAS*, 309, 750
 Dieguez, E. 1999, *Window Function Calculations for MINT*, Princeton Univ.
 Doriese, W. B. 2002, Ph.D. thesis, Princeton Univ.
 Gautier, T. N. I., Boulaner, F., Pérault, M., Puget, J.L. 1992, *AJ*, 103, 1313
 Goldin, A. B., et al. 1997, *ApJ*, 488, L161
 Grainge, K., et al. 2003, *MNRAS*, 341, L23
 Halverson, N. W., et al. 2002, *ApJ*, 568, 38
 Hawkins, D. W. 2003, “The COBRA Correlator System,” *URSI Conf. Proc.*, Boulder, Colorado
 Hobson, M. P., Lasenby, A.N., & Jones, M. 1995, *MNRAS*, 275, 863
 Hobson, M.P., & Maisinger, K. 2002, *MNRAS*, 334, 569
 Hunter, T. R., Wilson, R. W., Kimberk, R. S., Leiker, P. S., & Christensen, R. D. 2002, *Proc. SPIE*, 4848, 206
 Kerr, A. R., Pan, S.-K., Lichtenberger, A. W., Lloyd, F. L., & Horner, N. 1993, *Int. Symp. Space Terahertz Tech.* 4
 Kerr, A.R., Pan, S.-K., & Leduc, H.G. 1998, *Int. Symp. Space Terahertz Tech.* 9, 215 (also as MMA Memo 206)
 Kraus, J. D. 1986, *Radio Astronomy* (2d ed.; Powell, Ohio: Cygnus-Quasar)
 Lee, A. T., et al. 2001, *ApJ*, 561, L1
 Leitch, E. M., et al. 2002, *ApJ*, 568, 28
 Li, C. Q., Li, S. H., & Bosisio, R. G. 1984, *Microwave J*, 27, 125
 Matsushita, S., & Matsuo, H. 2003, *PASJ*, 55, 325
 Matthaei, G. L., Young, L., & Jones, E. M. T. 1980, *Microwave Filters, Impedance-Matching Networks, and Coupling Structures* (Dedham, MA: Artech House)
 Mauskopf, P. D., et al. 2000, *ApJ*, 536, L59
 Miller, A., et al. 1999, *ApJ*, 524, L1
 Miller, A., et al. 2002, *ApJS*, 140, 115
 Padin, S., et al. 2001, *ApJ*, 549, L1
 Padman, R. 1977, *Guide to the Design of Rectangular-to-Circular Waveguide Stepped Multi-Section Transitions*, RPP 2121(L), Division of Radiophysics, CSIRO, Sydney
 Page, L. A., et al. 2003, *ApJ*, 585, 566
 Plambeck, R. L., Thatte, N. A., & Sykes, P. B. 1993, *BAAS*, 25, 886
 Pospieszalski, M. W. 1992, in *Proc. IEEE Microwave Theory Tech. Soc., Microwave Symposium* (New York: IEEE), 1369;
 Pospieszalski, M. W., Lakatos, W. J., Nguyen, L. D., Lui, M., Liu, T., Le, M., Thompson, M. A., & Delaney, M. J. 1995, in *Proc. IEEE Microwave Theory Tech. Soc., Microwave Symposium* (New York: IEEE), 1121
 Pospieszalski, M. W. 1997, in *Proc. Moriond Astrophys. Meeting XVI, Microwave Background Anisotropies*, ed. F. R. Bouchet (Gif-sur-Yvette: Editions Frontiers), 23
 Robson, M., et al. 1993, *A&A*, 277, 314
 Ruhl, J. E., et al. 2003, *ApJ*, 599, 786
 Spergel, D. N., et al. 2003, *ApJS*, 148, 175
 Sunyaev, R. A., & Zel’dovich, Y. B. 1970, *Comments Astrophys. Space Phys.*, 2, 66.
 Sunyaev, R. A., & Zel’dovich, Y. B. 1972, *Comments Astrophys. Space Phys.*, 4, 173.
 Thompson, A. R., Moran, J. M., & Swenson, G. W. 1998, *Interferometry and Synthesis in Radio Astronomy* (2d ed.; Malabar, FL: Krieger)
 Toffolatti, L., Argueso Gomez, F., de Zotti, G., Mazzei, P., Franceschini, A., Danese, L., & Burigana, C. 1998, *MNRAS*, 297, 117
 Torbet, E., et al. 1999, *ApJ*, 521, L79
 Tran, H. T. 2002, Ph.D. thesis, Princeton Univ.
 Watson, R. A., et al. 2003, *MNRAS*, 341, 1057
 White, M., Carlstrom, J.E., Dragovan, M., & Holzapfel, W.L. 1999, *ApJ*, 514, 12